Soft Matter

PAPER

View Article Online
View Journal | View Issue

Cite this: *Soft Matter*, 2025, **21**, 8049

Combining SAXS analysis and MD simulation to determine structure and hydration of ionizable lipid hexagonal phases

Julian Philipp, †[a] Akhil Sudarsan,†[b] Ekaterina Kostyurina,[a] Viktoriia Meklesh,[c] Monica Berglund,[c] Michael Rappolt,[d] Jan Westergren,[e] Lennart Lindfors,[c] Nadine Schwierz[b] and Joachim O. Rädler *[a]

Cationic ionizable lipids (CILs) are fundamental components of inverse hexagonal (H_{II}) lipid assemblies, which mediate the encapsulation and release of negatively charged mRNA through a pH-dependent mechanism. Since variations in the structure and composition of the H_{II} phases can significantly impact the biological efficacy of the mRNA-carrying lipid nanoparticles (LNP), a comprehensive understanding of the ionizable lipid H_{II} phases is necessary. We present an integrated approach combining small-angle X-ray scattering (SAXS) experiments, molecular dynamics (MD) simulations and a continuum model to elucidate lipid distribution and water content within H_{II} phases. Our results indicate strong agreement between structures derived from MD simulations and SAXS data. To this end, we introduce a method to correct for periodic boundary artifacts when computing scattering profiles from MD simulations. This enables direct, model-free comparisons between experimental and simulated data, enhancing the reliability of structural interpretations, specifically the water content of the H_{II} phases. Next, we developed a continuum model to extend structural analysis to CIL H_{II} phases for which MD data is unavailable. This integrative framework not only provides molecular-level insights into the ionizable lipid H_{II} mesophase but also enables the prediction of hydration properties across different CIL compositions. The different approaches consistently yield water contents that seem to correlate with the lipids' transfection efficiencies. By bridging experimental and simulation data, our approach offers a powerful tool for the rational design and optimization of lipid nanoparticles, potentially linking a lower water content with an increased therapeutic performance.

Received 27th June 2025,
Accepted 20th September 2025

DOI: 10.1039/d5sm00666j

rsc.li/soft-matter-journal

1 Introduction

Lipid nanoparticles (LNPs) have emerged as powerful RNA delivery vehicles in modern medicine, with recent applications demonstrating their effectiveness in a wide range of drugs and vaccines. A critical component of efficient LNPs is the cationic ionizable lipid (CIL), which carries a pH-dependent charge at its head group. Although the optimal pK_a range for CILs in LNPs is well established (pH 6–7), *in vivo* transfection efficiencies can vary by up to two orders of magnitude, even among structurally similar CILs. This discrepancy highlights the importance of a deeper understanding of LNP structure to elucidate their intracellular release mechanisms, particularly during endosomal escape.[1–5]

LNPs are known to exhibit distinct mesophases depending on the local pH environment.[5–7] Among these, the inverse hexagonal (H_{II}) phase plays a key role in membrane fusion and cargo release. Although different CILs can form similar mesophases, subtle variations in structure can have a profound impact on transfection efficiency. In our previous work,[5] we demonstrated that bulk lipid phases composed of DLin-MC3-DMA (MC3), DLin-KC2-DMA (KC2), and DLinDMA (DD), in combination with cholesterol and water, undergo a pH-dependent structural transition from an inverse cubic micellar phase (*Fd3m*) to an inverse hexagonal (H_{II}) phase at approximately pH 6.0. Despite this shared transition point, significant differences in lattice spacing were observed between DD and the MC3/KC2 systems, suggesting distinct packing or hydration characteristics.

This underscores the need for a deeper analysis of these mesophases, with a particular focus on their water content, as

[a] *Faculty of Physics, Ludwig-Maximilians University, Geschwister-Scholl-Platz 1, Munich, Germany. E-mail: raedler@lmu.de*
[b] *Institute of Physics, University of Augsburg, Augsburg 86159, Germany*
[c] *Pharmaceutical Sciences, BioPharmaceuticals R&D, AstraZeneca, Gothenburg, Sweden*
[d] *School of Food Science and Nutrition, University of Leeds, Leeds LS2 9JT, UK*
[e] *Wendelsbergs beräkningskemi AB, Kyrkvägen 7B, 435 35 Mölnlycke, Sweden*
† JP and AS contributed equally to this work.

water content is relevant in RNA mobility, curvature energies as well as disruption occurring in pH-dependent structural transitions.

To gain a comprehensive understanding of lipid organization and hydration within LNPs, small-angle X-ray scattering (SAXS) experiments can be combined with molecular dynamics (MD) simulations. SAXS has significantly advanced our knowledge of lipid phase structures, particularly the inverted hexagonal H_{II} phase, which has been extensively studied as a model system.[8–10] Traditional SAXS data interpretation often relies on simplified models, such as Lorentzian peak-based structure factors and box model form factors. In contrast, more advanced Fourier-based analysis that reconstructs two-dimensional electron density maps, offer a more accurate and detailed view of the phase architecture.[11]

MD simulations have achieved significant progress in modeling large molecular systems like lipid mesophases and lipid nanoparticles. However, quantitative results rely heavily on the calibration of force fields and system parameters through experimental validation.[12–15] Previous studies on LNPs using coarse-grained force fields such as SPICA, which were meticulously optimized for lipid and nucleic acid systems, were able to closely reproduce experimental observations while providing molecular level insights into the pH-dependent structure of LNPs, thereby underscoring the importance of employing a rigorously validated force field.[16,17] Integrating experimental data not only refines and validates the simulations but also provides atomic-scale insights regarding water content,[5] ion interactions,[18] lipid structure[19] and lipid protonation.[20]

For easier interpretation, it is useful to describe the H_{II} phase using continuum models that describe the electron density profiles. Continuum models are characterized by interpretable parameters such as water content and area per lipid head group. A central challenge in developing such models is to minimize the number of free parameters while maintaining sufficient accuracy to capture the key structural features of the system. Simple models typically partition the phases into distinct, non-overlapping regions of water, lipid head groups, and lipid tails. More sophisticated approaches allow for overlapping Gaussian distributions to represent the spatial extent of each molecular component.[21,22]

In this study, we introduce a systematic methodology for structural analysis that integrates experimental SAXS data, MD simulations, and continuum model representations. Through an iterative refinement process, we align experimental and simulation data to produce a consistent and quantitative interpretation of lipid organization and hydration. Using this framework, we determine the water content of the inverse hexagonal phase formed by MC3, and extend our analysis to assess water content across a range of pH values and for additional ionizable lipids, including KC2, DD, and SM-102.

Our results reveal two key trends. First, the water content within the hexagonal phase appears to be largely invariant with respect to pH, indicating structural stability of hydration across physiologically relevant conditions. Second, we observe substantial differences in hydration among the different lipids: DD exhibits significantly higher water content than MC3 and KC2, while SM-102 shows a notably lower water content. This trend suggests a potential correlation between the hydration properties of CIL mesophases and their transfection efficiency when used in LNP formulations.[3,5] By offering a unified framework that links mesophase structure with functional performance, our approach provides valuable insights for the rational design and optimization of next-generation lipid nanoparticles.

2 Methods and model

2.1 Data analysis small angle X-ray scattering

Lipid bulk phase samples were prepared following the same procedure as explained in detail in our previous research.[5] In order to mimic the inner lipid phase of lipid nanoparticles, we mixed the cationic ionizable lipid (MC3/KC2/DD) with cholesterol at a 3 : 1 molar ratio in ethanol. The lipid mixture was filled into a dialysis cup together with a 50 mM citrate buffer at pH 3 creating a ethanol to water ratio of 2 : 1. Following dialysis steps first reduced the ethanol to water ratio to 1 : 3, then replaced the citrate–ethanol mixture with PBS buffer (1 mM KH_2PO_4, 155 mM NaCl, and 3 mM Na_2HPO_4, pH 7.4) and finally replaced it again with McIlvaine buffer (citric acid and disodium phosphate) at the desired final pH. For SM-102 we instead used citrate buffer (citric acid and sodium citrate) to adjust the pH. Each of these dialysis steps took 48 h to make sure that all the buffers in the dialysis cup were replaced and to give the sample material enough time to equilibrate to its new environment. These dialysis steps resulted in white precipitation that was extracted from the dialysis cup and sealed in quartz capillaries with 1.5 mm diameter together with an excess of the final buffer below and above the sample.

Small angle X-ray scattering (SAXS) patterns of the ionizable lipid bulk phases were recorded at the P12 EMBL BioSAXS[23] and the P62 SAXSMAT[24] beamlines at DESY. The angular calibration of the detector was performed with a silver-behenate reference sample. The resulting scattering patterns were radially integrated and background scattering was subtracted with reference measurements of empty capillaries.

For the inverted hexagonal H_{II} phase we found up to seven peaks (Fig. 1A). In order to get 2D electron density maps and radial scattering density profiles we closely followed the procedure described by Michael Rappolt and colleagues[11] but with a slight adjustment. Since the peaks were sharp and spaced out enough that there was no overlap between neighboring peaks, two distinct optimizations to the procedure were possible. Firstly we adjusted the background subtraction by calculating the background at each peak position individually. For each peak the background was determined with the measured intensity on both sides of the peak. Secondly, instead of fitting the peaks with Lorentz peak shapes first, we integrated the peaks above the background directly (grey area in insert of Fig. 1A). This way we could sum up all the scattering around a certain angle independent of the measured peak shape, which generally differs from an ideal Lorentz peak due to the

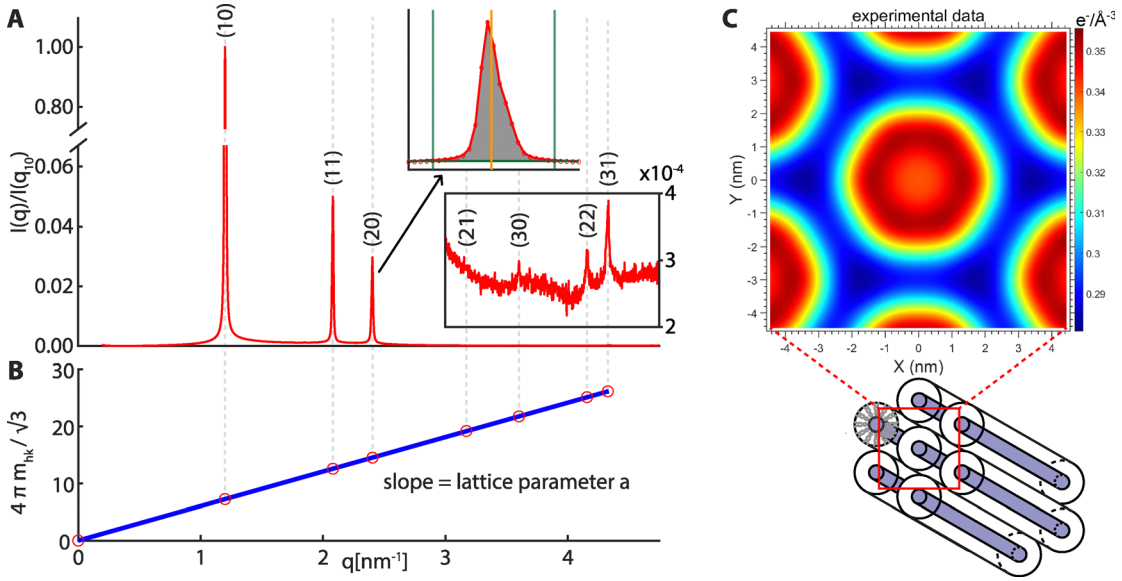

Fig. 1 Analysis of experimental SAXS data. (A) SAXS profile of the inverted hexagonal phase, normalized with the first peak height. Up to seven peaks could be measured and integrated for further analysis, although the later peaks are several magnitudes of order smaller than the first one. The insert shows the individual peak analysis. We define the peak intensity as the peak integral, independent of its exact shape. This is possible because the peaks are sharp enough not to overlap each other. The peak position is then the half-point of the integral, indicated by the orange line. (B) For each measurement the peak positions on the q scale are plotted against $\frac{4\pi}{\sqrt{3}}m_{hk}$. The slope of the linear fit through all points including the origin is the inverse hexagonal lattice parameter a. (C) The analysis of the lattice parameter and all peak intensities allows for the calculation of detailed 2D electron density maps of the inverse hexagonal lipid structure.

convolution of the direct beam profile (Gaussian distribution) with the diffraction peak contribution, arising from the inverse hexagonal phase.

After integrating each peak individually, we defined their positions to be where 50% of their total area is reached (orange line in insert of Fig. 1A). The lattice parameter a is determined as the slope when fitting $q_{hk} = \frac{4\pi}{\sqrt{3}}m_{hk}$ with $m_{hk} = \sqrt{h^2 + hk + k^2}$ and q_{hk} as the measured peak positions (Fig. 1B). The integrated peak areas were normalized regarding their multiplicity and a Lorentz correction was applied by multiplying each peak area by its corresponding m_{hk}^2. Finally, the square root of the corrected peak area was used to determine the form factor F of each peak. The electron density contrast was calculated by the same Fourier analysis as described by Michael Rappolt and colleagues:[11]

$$\Delta\rho(x,y) = \sum_{h,k\neq 0,0}^{h,k\,\max} \alpha_{h,k} \cdot F_{h,k} \cdot \cos(q_x(h,k)x) \cdot \cos(q_y(h,k)y). \quad (1)$$

$F_{h,k}$ is the peak amplitude (area) at position $q(h,k)$ with h and k as its respective Miller indices. The phase $\alpha_{h,k}$ for each peak is either +1 or 1. In order to find the right phase combination, we calculated the fourth moment of each phase combination following this formula from Mariani *et al.*:[25]

$$\langle(\Delta\rho)^4\rangle = (1/A)\int_A [\Delta\rho(r)]^4 \mathrm{d}r \quad \text{with} \quad \Delta\rho(r) = \rho(r) - \langle\Delta\rho\rangle. \quad (2)$$

A is the unit cell area, $\rho(r)$ the electron density at position r and $\langle\Delta\rho\rangle$ the average electron density. The correct peak phase combination generally has the lowest fourth moment. For almost all of our measurements (76 of 86) this is (+1, −1, −1, +1, +1, +1, +1) for the seven observed peaks. Only in a few cases either (+1, −1, −1, −1, +1, +1, +1) or (+1, −1, −1, −1, +1, +1, −1) had a slightly lower fourth moment. Those two alternatives can be disregarded since the resulting electron density maps show a 30° rotated hexagonal phase, which contradicts the assumption of an even tail region band between neighboring lipid tubes (Fig. S1). Therefore we used (+1, −1, −1, +1, +1, +1, +1) for all measurements, which is also in agreement with literature.[26,27] The result is a 2D electron density map (Fig. 1C), but without additional assumptions the electron density is not on an absolute scale.

2.2 MD simulations

All-atom MD simulations of inverse hexagonal H_{II} phases were performed for 1 μs using the GROMACS[28] software package. The starting structures for the simulation were generated using the CHARMM-GUI[29] web server and consisted of cationic MC3 lipids and cholesterol in a 3 : 1 molar ratio. The water content of the H_{II} phase was adjusted iteratively to match the experimental lattice spacing of 60 Å as reported in our previous work,[5] resulting in a ratio of 12 water molecules per lipid (Fig. 2A). A salt concentration of 0.15 M was introduced and additional ions were added to neutralize the system. A triclinic box with a length of 60 Å and a height of 91.4 Å was used to reproduce the symmetry of the H_{II} phase with the water column

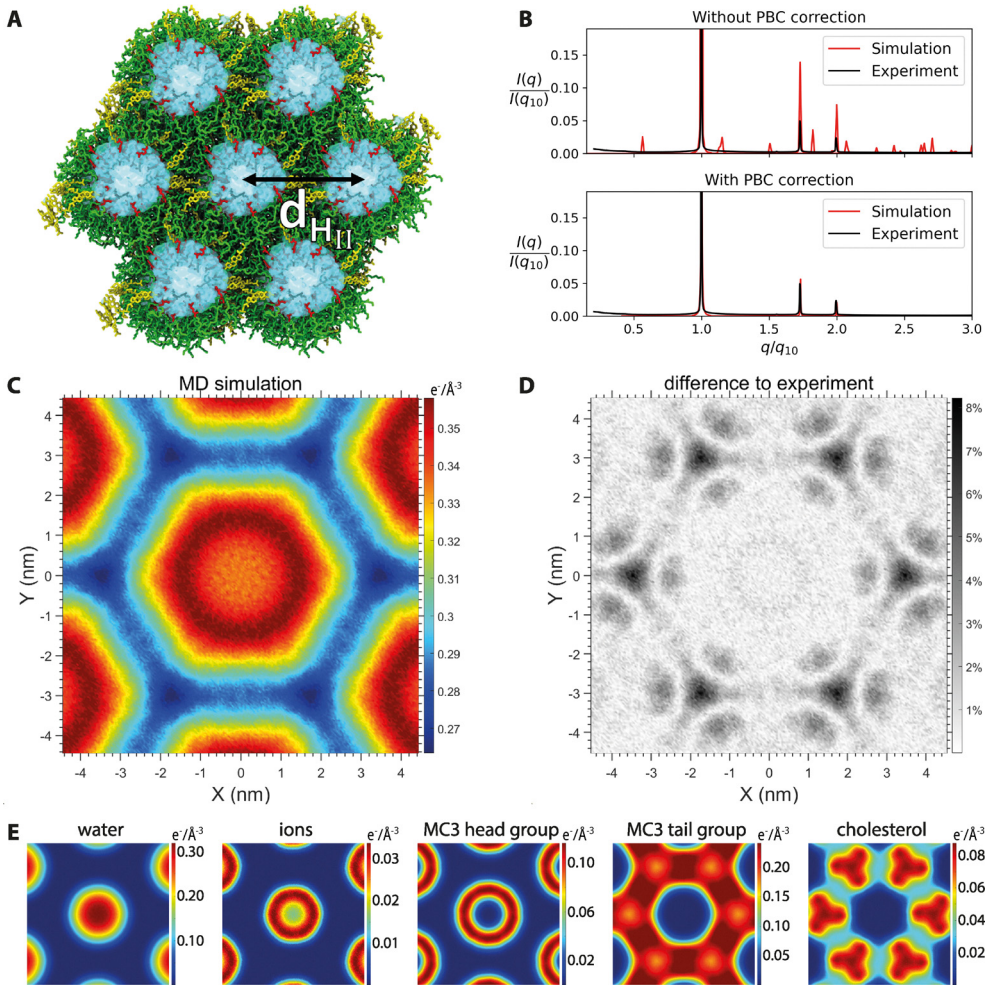

Fig. 2 Comparison of MD simulations and experimental data. (A) Simulation snapshot of the H_{II} phase. Water is shown in light blue, charged MC3 head groups in red, MC3 tails in green and cholesterol in yellow. $d_{H_{II}}$ indicates the distance between water columns. (B) Comparison of the scattering profiles obtained from MD simulations (red) and experiments (black) without periodicity corrections (top). After applying the methodology to correct scattering artifacts from periodic boundary conditions the simulated and experimental scattering profiles are in quantitative agreement (bottom) (C) 2D electron density profiles obtained from MD simulations. (D) Difference between the 2D electron density maps from simulations and experiments. (E) 2D electron density maps of the individual components obtained from the MD simulations. Higher resolution images are available in SI Fig. S4.

oriented along the *z*-axis. For the ionizable MC3 lipids, we used force field parameters, that were previously validated by neutron reflectometry and rigorously tested across multiple lipid phases, therefore the simulations focus exclusively on MC3 bulk phases.[19] For cholesterol, AMBER parameters derived from the lipid 17 force field[30] were used in combination with the TIP3P water model[31] and ion parameters from S. Mamatkulov & N. Schwierz.[32]

Following a steepest descent minimization, a 2 ns equilibration was performed to generate velocities and maintain the system at the desired temperature and pressure. The temperature was kept at 298 K using the Nose–Hoover thermostat with a time constant of 1.0 ps. The pressure was coupled semi-isotropically and maintained at 1.0 bar using the Berendsen barostat with a time constant of 1.0 ps. After equilibration a 1 μs production run was performed with a time step of 2 fs, keeping the former thermostat and employing the Parrinello–Rahman barostat with a time constant of 5.0 ps. van der Waals interactions and electrostatic interactions were cut-off at 1.2 nm and long-range electrostatics were evaluated using the particle Mesh Ewald method. The LINCS algorithm was used to constrain all bonds involving hydrogens. To correct for periodic boundary effects in the calculated scattering intensities, additional NVT simulations were carried out, which maintained a constant lattice spacing of 60 Å, as well as simulations of a multi-column system composed of 9 H_{II} columns in parallel, also simulated in the NVT ensemble. These simulations were 0.2 μs and 0.5 μs long respectively. The multi-column system was generated by extracting snapshots from the trajectory of a single H_{II} column at different time frames and combining them together in a 3 × 3 hexagonal lattice. A triclinic unit cell of length 180 Å and height 91.4 Å was used to define the periodic boundaries of the multi-column system. To avoid overlapping contacts and steric clashes, the larger system was energy minimized, equilibrated and simulated for 500 ns. A comprehensive list of all simulations performed in this study is

provided in the SI (see Table S1). VMD[33] was used to visualize and generate snapshots of the trajectory, while MDAnalysis[34,35] was employed to analyze the trajectory. Generation of 2D electron density maps perpendicular to the *Z*-axis (*i.e.* the water column orientation) from the simulation trajectory (discarding the first 100 ns for equilibration) for the whole system and the individual components were done by MDAnalysis scripts.

2.2.1 Scattering intensity from MD. Molecular dynamic simulations provide a detailed temporal and spatial mapping of atomic coordinates, enabling a direct and straightforward computation of the theoretical scattering profiles from atomic positions. Mercury CCDC (Cambridge Crystallographic Data Centre) was used to calculate the X-ray scattering profiles from the MD simulations. The simulated X-ray scattering profiles were generated using the Cu-K_α radiation source of wavelength λ = 1.54056 Å for a 2θ range of 0.7–7°. Here, the scattering angle θ is related to the momentum transfer vector q *via* $q = \frac{4\pi}{\lambda}\sin(2\theta/2)$. The simulated H_{II} phases were assumed to have a crystalline size of 1130 nm by fixing the broadness of the scattering peaks to 0.00781°. The peak width, defined by the full width at half maximum (FWHM), is related to the crystal domain size by the Scherrer equation. The random orientation of individual crystals are taken into account by using the powder diffraction technique.

However, additional peaks in the theoretical scattering profiles are observed due to the periodicity of the molecular system. MD simulations are typically performed using finite nanometer sized simulation boxes with periodic boundary conditions to mimic macroscopic systems. By construction, the initial system is identical to its periodic images. However, the periodic repetition leads to constructive interference at q values inversely proportional to the size of the simulation box. These scattering artifacts appear as additional peaks in the scattering profile (Fig. 2B). To remove these artifacts, a methodology tailored to the H_{II} lipid phase was formulated and is presented below.

2.2.2 Removal of scattering artifacts from periodic boundary conditions. Given that periodic boundary conditions are applied along *x*, *y* and *z* directions in the 3D lattice, it is necessary to correct for the scattering artifacts arising in all three directions. We start by defining the *Z* axis as the direction parallel to the water column. To remove the additional interference peaks due to the periodicity along the *Z* direction, scattering profiles are calculated from the same NVT simulations but with a reduced box size of 5, 10 and 15% of the original system respectively. For a reduced box size, the position of the peaks shift to higher q values (*e.g.* for $L' = (9/10)L$ the peak at q will appear at $q' = (10/9)q$, see Fig. S2A). By contrast, the position of the peaks reflecting the hexagonal symmetry (q_{10}, q_{11} and q_{20}) remain at the same position. The corrected intensity profile is obtained by removing the shifting peaks and taking the minimum intensity at the symmetry peaks.

Artifacts arising from the periodicity in the *XY* plane are addressed by tiling the system along the *XY* plane, resulting in the creation of a multi-column H_{II} phase. Since the first three peaks of the H_{II} system appear at $q/q_{10} = 1, \sqrt{3}$ and 2, the box size has to be tripled to avoid overlap of the artifact peaks with the symmetry peaks. We calculate the scattering profile for the full 3 × 3 system and for a single subsystem. For the multi-column system with $L' = 3L$, the symmetry peaks split. For example, the q_{11} peak is shifted to lower q values with $q' = 1/3q$ (see Fig. S2B). The corrected intensity profile is again obtained by removing the shifting peaks and taking the minimum intensity at the symmetry peaks. Note that the q_{30} peak will still contribute to the q_{10} peak after tripling the system. However, since its intensity is very low the contribution is neglected. Finally, the scattering profiles were calculated for 20 distinct molecular snapshots sampled from the NVT simulation trajectory (Fig. S3).

2.3 Continuum model of the lipid–water interface

With the MD simulations we are able to calculate the water content of the MC3 bulk phase but for many different ionizable lipids there is no force field data available, so at the moment it is impossible to extend the MD simulations to those as well. In order to generalize the model without the need for extensive and lipid specific MD simulations, we developed a numerical continuum model that can be easily extended to different ionizable lipids as well. The model uses parameters calculated with ACD ChemSketch from literature data and fits radial scattering length density (SLD) distributions of water molecules as well as the lipid head- and tail-groups to a total SLD profile. The radial electron density curves can be converted to SLD profiles because for X-rays the SLD is proportional to the electron density. This generally enables the calculation of water content in inverse hexagonal lipid phases without the need for associated MD simulations.

The parameters calculated with ACD ChemSketch[36] are the molecular volumes of the lipid head group V_{head} and tail group V_{tail}. The scattering length density SLD_{tail} was calculated using SasView 6[37] (see Table 1).

The SLD of water is taken from literature (SLD_{water} = 9.45 × 10^{-4} nm^{-2}).[38] This continuum model assumes smooth distributions for water and lipid tail groups of a distinct shape based on the distributions observed in our MD simulations. The head group distribution is defined so that at each radius the volume fractions of all components add to one.

In detail the distribution base function of the water core is defined as

$$f_{water,base}(r) = \exp\left(-\ln(2)\left(\frac{r}{b_w}\right)^{\alpha_w}\right), \quad 0 < r < \frac{d}{2} \qquad (3)$$

Table 1 Continuum model parameters calculated with ACD ChemSketch[36] and SasView 6[37]

CIL	V_{head}[a] [nm^3]	V_{tail}[b] [nm^3]	SLD_{tail}[b] [10^{-4} nm^2]
SM-102	0.411	0.862	7.46
MC3	0.183	1.019	8.02
KC2	0.184	1.019	8.02
DD	0.123	1.039	7.70

[a] Head group definitions: SM-102 $C_{16}H_{29}NO_5$, MC3 $C_6H_{13}NO_2$, KC2 $C_7H_{15}NO_2$, DD $C_5H_{13}NO_2$. [b] Tail group definitions: SM-102 $C_{28}H_{60}$, MC3 $C_{37}H_{68}$, KC2 $C_{37}H_{68}$, DD $C_{36}H_{68}$.

with r as the radial variable, d as the center-center distance of two neighboring water cylinders and both b_w and α_w as fitting parameters. Similarly the distribution base function of the lipid tail groups is defined as

$$f_{\text{tail,base}}(r) = \exp\left(-\ln(2)\left(\frac{r-d/2}{b_t}\right)^{\alpha_t}\right), \quad 0 < r < \frac{d}{2} \qquad (4)$$

with α_t as an additional fitting parameter. b_t is not a free parameter but is used to adjust the ratio of volume fractions of head groups and tail groups to the same ratio as their molecular volumes in order to have the same number of head and tail groups.

These base functions have to be stretched depending on the angle θ up to $r = \frac{d}{\sqrt{3}}$ to account for the hexagonal shape of the unit cell. The stretched functions are then integrated over θ to get back to a pure radius dependency. Refer to the SI for more details. Since the distribution functions must add to unity everywhere, the stretched radial distribution of the head groups is then defined as

$$f_{\text{h,stretched}}(r) = 1 - \left(f_{\text{w,stretched}}(r) + f_{\text{t,stretched}}(r)\right) \quad \text{with} \quad 0 < r < \frac{d}{\sqrt{3}} \qquad (5)$$

The stretched distribution functions are then multiplied by their respective molecular SLD and added together for all three components. By adjusting the fitting parameters b_w, α_w, α_t as well as the molecular SLD of the lipid head group SLD_{head}, the model can be fitted to SLD profiles and allows for the calculation of the volume fractions of its components like the water volume fraction ϕ_w. SLD_{head} could also be calculated by ACD ChemSketch, but the model only fits properly if SLD_{head} is left as a fitting parameter. This is a slight imperfection of the model, but might be caused by the changing charge of the head group depending on the pH and buffer.

Additionally the area per head group S can be calculated according to M. W. Tate & S. M. Gruner[39] using

$$S = \frac{2V_{lip}\phi_w}{b_w(1-\phi_w)} \qquad (6)$$

V_{lip} is the lipid volume ($V_{lip} = V_{head} + V_{tail}$, see Table 1) and b_w is the radius at which the water distribution reaches 50% of its maximum value (see eqn (3)).

2.4 Dynamic vapor sorption

To validate the water contents derived from the combined continuum model/SAXS approach we aim to determine water content using an alternative experimental technique. Dynamic vapor sorption (DVS) is a gravimetric technique used to measure the amount of water absorbed or desorbed by a sample. The technique involves suspending the sample on a highly sensitive microbalance in a temperature-controlled chamber followed by systematic regulation of the relative humidity (%RH) by a mass flow controller. The %RH is changed once the sample reaches a state of equilibrium moisture content (EMC) where there is no longer any change in the amount of water absorbed/desorbed by the sample. EMC is defined as the ratio of water weight to dry weight of the sample and is plotted against %RH to obtain vapor sorption isotherms. Empty bulk phases of DLin-MC3-DMA, DLin-KC2-DMA and DLinDMA at pH 5.5 were prepared using the sequential buffers: 50 mM citrate pH 3.0, PBS pH 7.4 and McIlvaines buffer 5.5. DVS analysis was performed using an instrument from surface measurement system, DVS resolution. A bulk phase sample (approximately 15–25 mg) was transferred to a tared sample holder. The instrument was purged with nitrogen, 200 mL min^{-1}, at 25 °C and data was collected at different %RH. Starting at 95%RH and going stepwise down to 80%RH, using 2.5%RH steps and finally to 0%RH to obtain the dry weight of the sample. The %RH was changed manually when the equilibrium was reached and the signal showed no drift. From the measure weights and the dry weight together with density of each lipid the water volume fraction was calculated against %RH. The extrapolation to 100%RH was carried by deriving eqn (7) below.[40]

$$\phi_w(a_w) = \frac{a_w\phi_w}{a_w\phi_w + \frac{(1-\phi_w)(1-a_w q)(1+a_w(q_i-q))}{(1-q)(1+q_i-q)}} \qquad (7)$$

in which a_w = water activity (%RH/100), ϕ_w = water volume fraction at $a_w = 1$, and q_1 and q, from the statistical weights of the first layer ($a_w q_1$) and all other layers ($a_w q$), were treated as fitting parameters.

This extrapolation generally exhibits large margins of error but it is necessary since going beyond 95%RH could cause condensation on the sample. Additionally, obtaining data for a single point on the isotherm requires a significant amount of time, making this approach impractical for a large number of samples. While DVS is not a flawless technique, it can serve as a useful experimental tool to validate and complement the results obtained from the combined MD-SAXS approach.

3 Material

DLin-MC3-DMA (*O*-(*Z*,*Z*,*Z*,*Z*-heptatriaconta-6,9,26,29-tetraem-19-yl)-4-(*N*,*N*-dimethylamino) butanoate; $C_{43}H_{79}NO_2$; mw 642.09 g mol^{-1}; >99% purity), DLin-KC2-DMA (2,2-dilinoleyl-4-(2-dimethylaminoethyl)-[1,3]-dioxolane; $C_{43}H_{79}NO_2$; mw 642.09 g mol^{-1}; >99% purity), and DLinDMA (1,2-dilinoleyloxy-3-dimethylaminopropane; $C_{41}H_{77}NO_2$; mw 616.06 g mol^{-1}; >99% purity) were synthesized at AstraZeneca.

Cholesterol ($C_{27}H_{45}OH$; 386.66 g mol^{-1}; >98% purity), potassium phosphate monobasic (KH_2PO_4; >99% purity), sodium chloride (NaCl; >99% purity), disodium phosphate (Na_2HPO_4; >99% purity), citric acid ($C_6H_8O_7$; >99.5% purity), sodium citrate dihydrate ($C_6H_5Na_3O_7{\cdot}2H_2O$; >99% purity), and ethanol (C_2H_6O; >99.5% purity) were purchased from Sigma-Aldrich.

4 Results

4.1 Validation of the MD simulations

To validate and test the reliability of the MD simulations, we compare the water content obtained from the MD simulations with the experimental water content and the spatial distribution of the ionizable lipids and cholesterol around the water column.

4.1.1 Volume fraction of water. The water content in our MD simulations were calculated using three different methods. The first method involved calculating the water volume fraction ϕ_w from the radial distributions as described in our previous work.[5] The second method assumes an empirical water volume of 30 Å^3 to calculate the volume fraction based on the number of water molecules in the simulation box.

The third method utilizes the procedure developed by Petrache *et al.*[41] to generate the volume fractions and molecular volumes of the components that make up the H_{II} system (see SI Section S4 for further details). The resulting molecular volumes obtained for the individual components MC3, cholesterol and water are 1190 Å^3, 632.7 Å^3 and 28.7 Å^3 respectively. Using a three component splitting (MC3, cholesterol, water + ions) resulted in the water + ions component having a molecular volume of 29.9 Å^3. Based on these molecular volumes, the volume fraction of individual components were calculated and are listed in Table 2.

The computationally derived water content aligns closely with the experimental measurement as we show below, suggesting that the MD simulations provide an excellent representation of the system.

4.1.2 Electron densities and scattering profiles from MD simulations. To further validate the molecular model employed in the MD simulations, we directly compared the scattering intensities (Fig. 2B) and the two-dimensional (2D) electron density maps obtained from simulations and experiments (Fig. 2C and D). The corrected theoretical scattering profiles exhibit excellent quantitative agreement with the experimental data, accurately reproducing the measured intensities within the experimental errors (Fig. 2B, bottom). It is important to note, however, that this level of agreement is only achieved after correcting for scattering artifacts introduced by the periodic boundary conditions inherent to the MD simulations (see Section 2 for details).

The 2D electron density maps from the simulations and the experiments exhibit a characteristic hexagonal symmetry, with a prominent ring of highest electron density surrounding the central water tube (Fig. 2). The differences between the simulated and experimental electron density maps are minimal, indicating strong agreement in the 2D spatial distributions. This concordance is consistent with the previously observed similarity in the scattering intensities (Fig. 2B). Note that the noise level in the experimental electron density map is lower compared to the simulations due to the smooth interpolation used. The electron densities obtained from the MD simulations can be split into electron densities of the individual components (Fig. 2E and Fig. S5). Interestingly the distribution of dissolved ions does not completely follow the distribution of water, but forms a ring of highest density close to the MC3 head groups, attracted by its charges. Most of the distributions are radially symmetric except cholesterol and the MC3 tails. In order to fill the gaps between three water channels, the MC3 tails have to stretch, causing a shift from a round to a hexagonal shape in the total electron density. Additionally in our experiments we see that the excess of cholesterol in our system phase separates as large crystals of cholesterol monohydrate. These are both often visible in our SAXS data as a sharp peak at q = 1.85 Å^{-1} and as quadrangular platelets in microscopy data. In the MD simulations this effect is not taken into account and the cholesterol content is therefore likely overestimated. Here, the cholesterol accumulates in the corners between three water cylinders, which probably causes the difference between MD simulation and experimental data at this location (Fig. 2D).

In addition to the 2D electron density maps, generation of theoretical X-ray scattering profiles from MD simulation achieves direct comparison with the experimental scattering profiles. However prior correction of scattering artifacts are necessary as per the procedure described in the Methods section. The corrected theoretical scattering profiles exhibit excellent quantitative agreement with the experimental scattering profiles, reproducing the experimental intensities within the error of the simulations (Fig. 2B).

In summary, the scattering intensities (Fig. 2B) and 2D electron density maps (Fig. 2C and D) derived from simulations and experiments show remarkably good agreement, highlighting recent advancements in molecular modeling[5,19] and underscoring the importance of direct, quantitative comparisons between simulated and experimental data. To model the low pH conditions that favor the H_{II} phase, we assumed full protonation of the ionizable lipid residues. However, it is possible that the actual protonation degree in the complex lipid environment is lower.[20] Despite this simplification, the close agreement between simulated and experimental scattering profiles and electron densities supports the accuracy and robustness of the molecular model.

Table 2 Volume fractions of different components of the system obtained using three different approaches

Component	ϕ_w (method 1)	ϕ_w (method 2)	ϕ_w (method 3)
MC3	63.0%	—	62.3%
Cholesterol	12.3%	—	11.1%
Water	24.0%	25.1%	24.0%
Water + ions	24.6	—	26.5%

4.2 Validation of the continuum model

Validation of our continuum model was realized in two independent ways. The first one is by applying the model to total SLD profiles from MD simulations for MC3 bulk phases at different water contents (see Table 3). To obtain meaningful and controlled validation, the MC3 bulk phase in the MD simulations was assumed to be fully protonated, given that

Table 3 Validation of continuum model against different MD simulations by comparing the water content. Adjusting the MD simulation to the lattice spacing of our experimental data led to 12 water molecules per CIL[5]

Water molecules/CIL	ϕ_w (MD simulation) (%)	ϕ_w (continuum model) (%)
12	24.6	25.5
13	25.3	25.6
18	32.6	32.7

the exact protonation states of MC3 in lipid mesophases at specific pH conditions remain unknown. In order to avoid differences caused by cholesterol in the three channel corner in the range $d/2 < r < d/\sqrt{3}$, we took the SLD profiles in the direction towards the nearest neighboring water channel center. Here the radial electron density profiles of experimental data and MD simulation match quantitatively. From the MD simulations we are able to split the total electron density profile into three distinct components: the water including its dissolved ions, the MC3 head group and the MC3 tails including cholesterol (Fig. 3). Both water contents agreed in all three comparisons with less than one percent difference.

We then applied the continuum model to the total SLD profiles from our experimental data as shown in Fig. 4A. The continuum model fits the SLD profile extracted from experimental data almost perfectly by adding the shown distributions of water molecules, lipid head groups and lipid tail groups together. This allows us to calculate the water content for MC3 bulk phases at different pH values as well as for three additional ionizable lipids: DLin-KC2-DMA (KC2), DLinDMA (DD) and SM-102.

According to our continuum model, DD has the highest water content of 32.0 ± 2.5%, followed by KC2 (24.7 ± 1.1%) and MC3 (24.7 ± 1.0%). The water content of MC3 was consistent with the value obtained from MD simulations (24.6%). SM-102 has the lowest water content with only 16.2 ± 2.0%. The calculated water contents are independent of pH within the margins of error. There is a small trend of reducing water content with increasing pH for DD, but the margins of error are too big for the trend to be significant.

The second approach to validate our continuum model is by comparing these results to DVS measurements. The extrapolated water volume fractions from DVS measurements for MC3, KC2 and DD lipids are 22.8 ± 1.7%, 24.6 ± 0.9% and 25.4 ± 0.8% as shown in Fig. 4B. Even though the observed trends in water content are consistent with the continuum model, minor deviations in magnitude with the expected water volume fractions are observed. This may be due to the reliance on extrapolation to 100%RH from a limited number of data points obtained from the time-intensive DVS measurements, further highlighting the importance of integrating multiple computational and experimental methodologies to achieve reliable and consistent outcomes. An overview of the calculated water content for all four lipids as well as the results from DVS and MD are presented in Fig. 4C.

The average area per head group over our pH range, weighted by their inverse errors, is for SM-102 0.57 ± 0.5 nm^2, followed by MC3 (0.54 ± 0.2 nm^2), KC2 (0.53 ± 0.2 nm^2) and DD (0.51 ± 0.3 nm^2) (see Fig. 4D). The area per head group is mostly pH independent for MC3 and KC2 within their margins of error. SM-102 seems to have a decreasing area per head group with decreasing pH, but a constant area is also possible within the margins of error. Only DD has an increasing area per head group with decreasing pH.

The average hexagonal lattice spacing is the lowest for SM-102 with only 4.50 ± 0.13 nm, followed by MC3 with 6.01 ± 0.07 nm, KC2 with 6.10 ± 0.06 nm and DD with 7.62 ± 0.22 nm.

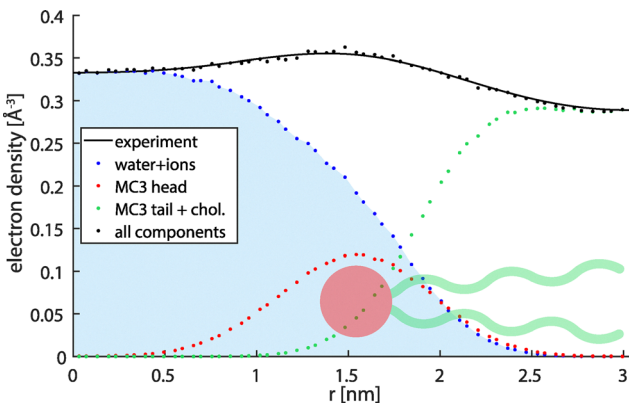

Fig. 3 Total scattering length density (SLD) and splitting into components. Radial electron density profile in the direction towards a neighboring water channel, starting from the center of the water tube at r = 0. The electron densities are split further into individual components.

5 Discussion and conclusions

The combination of experimental SAXS data and MD simulations enables the determination of water content in inverse hexagonal bulk phases containing MC3. With the addition of the proposed continuum model and additional SAXS measurements the water content of different inverse hexagonal bulk phases is estimated. We find a defined order of water content as a function of CIL with DLinDMA (DD) > DLin-MC3-DMA (MC3), DLin-KC2-DMA (KC2) > SM-102. The order is inversely correlated to the reported transfection efficiencies[3,5] that follow DLinDMA (DD) < DLin-KC2-DMA (KC2), DLin-MC3-DMA (MC3) < SM-102. The observed systematic trend hints towards a possible functional link between both properties. In general, our combined structural analysis allows for measurement of the water content of any CIL bulk phase that exhibits H_{II} bulk phase based on SAXS data and the proposed continuum model. Following the proposed structure–function relation, water content together with a pH-sensitive phase transition could possibly prove to be a reliable indicator of transfection efficiency.

The continuum model developed here should be useful as a close proxy of the electron density profile for the lipid and water moiety. However, while the model shows good agreement with MD simulations it does still exhibit slight imperfections. The necessity to use the head group scattering length density

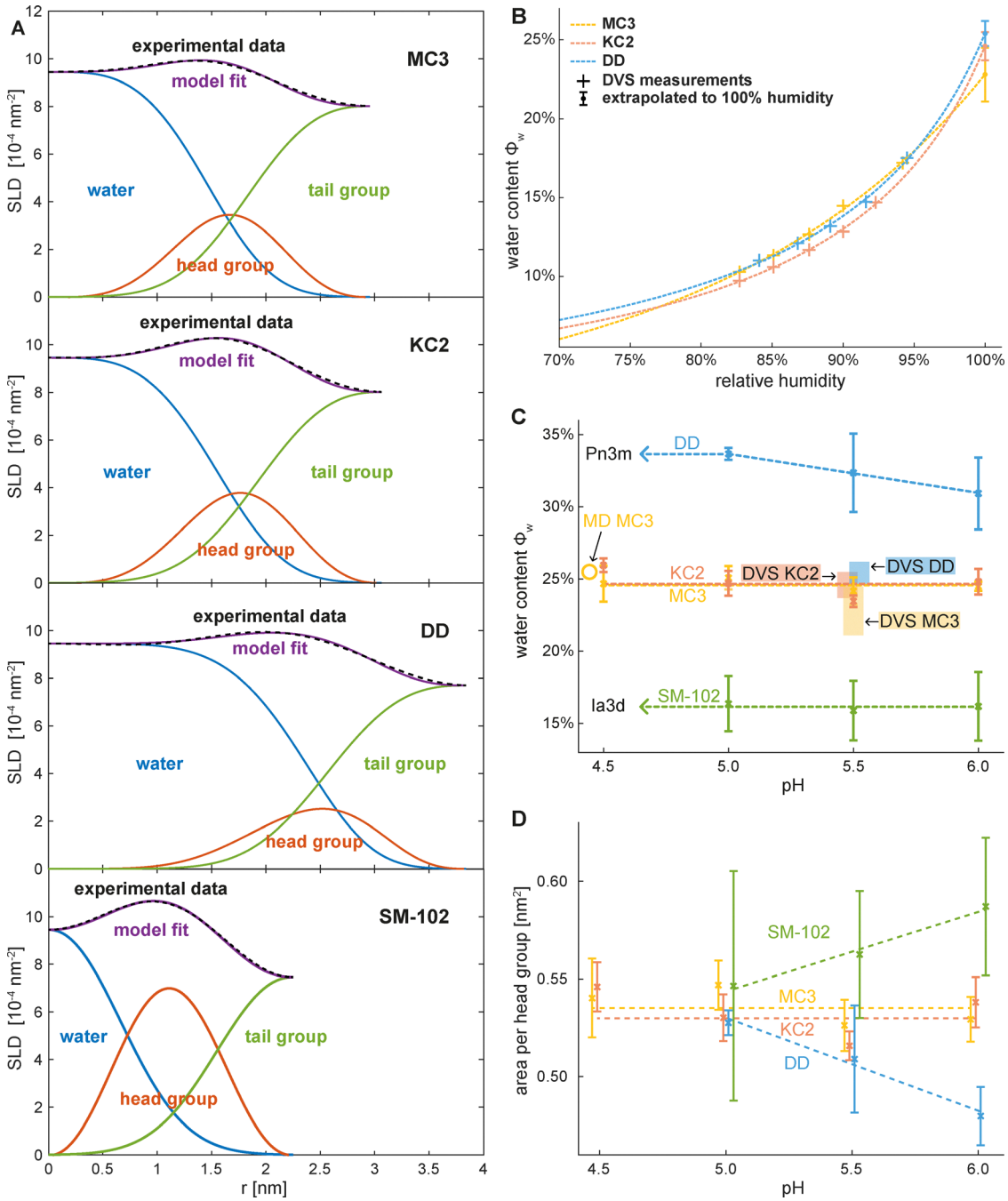

Fig. 4 Application of continuum model on SLD profiles of experimental data and results. (A) Radial SLD profiles from experimental data of MC3, KC2, DD, and SM-102, here shown as a dashed black lines, are fitted by continuum model (purple) which consists of the water distribution (blue), head group distribution (red) and tail group distribution (green). (B) Dynamic vapor sorption (DVS) measurements of MC3, KC2 and DD at pH 5.5 are extrapolated to 100% relative humidity resulting in estimated water contents for MC3 (22.8 ± 1.7%), KC2 (24.6 ± 0.9%) and DD (25.4 ± 0.8%). (C) Summarized results from the continuum model, DVS measurements and MD simulations. The DVS measurements of DD do not agree with our continuum model within their margins of error which might be due to the reliance on extrapolation to 100%RH from a limited number of DVS data points. According to our continuum model SM-102 has the lowest water content with 16.2 ± 2.0%, followed by MC3 (24.7 ± 1.0%) and KC2 (24.7 ± 1.1%). DD has the highest water content and is the only lipid that increases its water content with decreasing pH. The MD simulation with fully ionized MC3 was calibrated to 24.6% water content. Below pH 5.0 the bulk phases of SM-102 and DD transition from the H_{II} phase to bicontinuous phases (*Ia3d* and *Pn3m*). (D) The area per lipid head group within the H_{II} phase was calculated with our continuum model. Dotted lines are added as a guide to the eye. Within their margins of error the area per head group is independent of pH for MC3 and KC2. For SM-102 it displays an increasing area per head group with increasing pH and for DD the area is decreasing.

SLD_{head} as a fitting parameter although it could instead be calculated with ACD ChemSketch indicates inaccuracies of the fit. Our MD simulations themself show also slight differences compared to experimental data coming from the cholesterol

distribution. From experiments we know that excessive cholesterol forms large cholesterol monohydrate crystals that grow orders of magnitude larger than the lipid structure unit cells making it impossible to be accurately simulated. Although these cholesterol crystals are probably not part of the actual bulk phase inside lipid nanoparticles, its obvious excess makes it difficult to predict the correct amount of cholesterol for the simulations.

Initially, we expected to observe an electrostatically driven swelling of the ionizable mesophases at lower pH, caused by the increasing charge of the head groups. Such behavior is well documented for ionizable lamellar phases. However, swelling of the hexagonal phases was barely detectable and only observed for DD. In contrast, SM-102 even showed the opposite trend, though within large margins of error. Furthermore, the bulk phase water content of all lipids except DD appeared to be independent of pH. For DD, a slight increase in water content with decreasing pH was observed, which can be explained by the reduced absolute curvature resulting from the increasingly charged head groups.

We propose that the spacing of hexagonal phases is largely insensitive to pH because the elastic curvature energy of the lipid tail region dominates over electrostatic contributions of the head group. In other words, the energetic cost of lipid deformation prevents electrostatic swelling of the hexagonal phase. This interpretation aligns with our hypothesis that the micellar-to-hexagonal phase transition of the excess lipid fraction in LNPs is critical in the initial endosomal fusion process. In this context, it is noteworthy that the elastic energy depends strongly on curvature, which would explain why ionizable lipid mesophases with high curvature, *i.e.* small hexagonal lattice spacing or low water content, are more potent to drive fusion than those with lower curvature (larger spacings), such as DD.

Compared with DD, all the other tested lipids form denser structures; notably SM-102 has the lowest water content and highest transfection efficiency. We speculate that the micellar-to-hexagonal transition at decreasing pH values initiates the onset of fusion due to the rearrangements in topological discontinuous structures. Note that, while fusion disrupts the endosomal compartment, it does not necessarily coincide with the release of mRNA from its hexagonal complexed phase. The mRNA–lipid salt complex is likely to dissolve more gradually once released into the cytosol.

In summary, SAXS analysis combined with MD simulations and a newly derived continuum model has proven to be a reliable method to determine the water content of inverse hexagonal bulk phases. The approach can be extended to other ionizable lipids that show H_{II} bulk phase signatures in SAXS. The bulk phase water content, along with the pH-dependent phase transition behavior of ionizable lipids, are critical parameters for estimating their transfection efficiency in future applications.

Author contributions

L. L., N. S. and J. O. R. designed research; J. P., E. K., V. M., and M. B. performed research; A. S. and N. S. performed simulations; J. P., A. S., E. K., V. M., M. B., and J. W. analyzed data and J. P., A. S., N. S., M. R., J. W., L. L., N. S., and J. O. R. wrote the paper.

Conflicts of interest

V. M., M. B., and L. L. are employed by AstraZeneca R&D Gothenburg.

Data availability

Raw SAXS data can be accessed *via* DOI: **10.5282/ubm/data.689**.

Additional information and high resolution images can be found in the supplementary information (SI). Supplementary information is available. See DOI: **https://doi.org/10.1039/d5sm00666j**.

Acknowledgements

This work was supported by the German Federal Ministry of Education and Research through BMBF Project 05K18WMA and 05K18EZA within the framework of the Swedish–German research collaboration Röntgen-Ångström Cluster as well as by the Deutsche Forschungsgemeinschaft (Project No. 201269156, SFB1032-B01). The authors gratefully acknowledge the scientific support and HPC resources provided by the Erlangen National High Performance Computing Center (NHR@FAU) of the Friedrich-Alexander-Universität Erlangen-Nürnberg (FAU) under the NHR project b119ee and b253ee. NHR funding is provided by federal and Bavarian state authorities. NHR@FAU hardware is partially funded by the German Research Foundation (DFG) – 440719683. Deutsches Elektronen-Synchrotron (DESY) P12 BioSAXS EMBL and P62 SAXSMAT beamlines at PETRA III (Hamburg, Germany), and the beamline scientists Clement E. Blanchet and Xiao Sun are greatly acknowledged for synchrotron beamtime. M. R. is particularly grateful for the support provided by Gerome Vancuylenberg in the initial analysis of the electron density maps, who has been supported by the EPSRC scholarship grant (EP/S023631/1). This work also benefited from the use of the SasView application, originally developed under NSF award DMR-0520547. SasView contains code developed with funding from the European Union's Horizon 2020 research and innovation programme under the SINE2020 project, grant agreement no 654000. This manuscript is dedicated to Erich Sackmann, who pioneered lipid membrane biophysics and advised structural research on biological systems using X-ray and neutron scattering.

Notes and references

1 P. R. Cullis and M. J. Hope, *Mol. Ther.*, 2017, **25**, 1467–1475.
2 M. Jayaraman, S. M. Ansell, B. L. Mui, Y. K. Tam, J. Chen, X. Du, D. Butler, L. Eltepu, S. Matsuda, J. K. Narayanannair, K. G. Rajeev, I. M. Hafez, A. Akinc, M. A. Maier, M. A. Tracy,

P. R. Cullis, T. D. Madden, M. Manoharan and M. J. Hope, *Angew. Chem., Int. Ed.*, 2012, **51**, 8529–8533.
3 K. J. Hassett, K. E. Benenato, E. Jacquinet, A. Lee, A. Woods, O. Yuzhakov, S. Himansu, J. Deterling, B. M. Geilich, T. Ketova, C. Mihai, A. Lynn, I. McFadyen, M. J. Moore, J. J. Senn, M. G. Stanton, Ö. Almarsson, G. Ciaramella and L. A. Brito, *Mol. Ther.–Nucleic Acids*, 2019, **15**, 1–11.
4 G. Tesei, Y.-W. Hsiao, A. Dabkowska, G. Grönberg, M. Y. Arteta, D. Ulkoski, D. J. Bray, M. Trulsson, J. Ulander, M. Lund and L. Lindfors, *Proc. Natl. Acad. Sci. U. S. A.*, 2024, **121**, e2311700120.
5 J. Philipp, A. Dabkowska, A. Reiser, K. Frank, R. Krzysztoń, C. Brummer, B. Nickel, C. E. Blanchet, A. Sudarsan, M. Ibrahim, S. Johansson, P. Skantze, U. Skantze, S. Östman, M. Johansson, N. Henderson, K. Elvevold, B. Smedsrød, N. Schwierz, L. Lindfors and J. O. Rädler, *Proc. Natl. Acad. Sci. U. S. A.*, 2023, **120**, e2310491120.
6 Z. Xu, J. M. Seddon, P. A. Beales, M. Rappolt and A. I. I. Tyler, *J. Am. Chem. Soc.*, 2021, **143**, 16556–16565.
7 J. M. Seddon, *Cells*, 2025, **14**, 716.
8 M. Rappolt, A. Hickel, F. Bringezu and K. Lohner, *Biophys. J.*, 2003, **84**, 3111–3122.
9 B. Kollmitzer, P. Heftberger, M. Rappolt and G. Pabst, *Soft Matter*, 2013, **9**, 10877.
10 Š. Perutková, M. Daniel, M. Rappolt, G. Pabst, G. Dolinar, V. Kralj-Iglič and A. Iglič, *Phys. Chem. Chem. Phys.*, 2011, **13**, 3100–3107.
11 G. Vancuylenberg, A. Sadeghpour, A. I. I. Tyler and M. Rappolt, *Soft Matter*, 2023, **19**, 8519–8530.
12 M. F. Trollmann and R. A. Böckmann, *Biophys. J.*, 2022, **121**, 3927–3939.
13 W. Wang, S. Feng, Z. Ye, H. Gao, J. Lin and D. Ouyang, *Acta Pharm. Sin. B*, 2022, **12**, 2950–2962.
14 A. Hardianto, Z. S. Muscifa, W. Widayat, M. Yusuf and T. Subroto, *Molecules*, 2023, **28**, 4836.
15 X. Fernandez-Luengo, J. Camacho and J. Faraudo, *Nanomaterials*, 2017, **7**, 461.
16 A. P. Singh, H. Tanaka, Y. Miyazaki, S. Nagano and W. Shinoda, *J. Chem. Theory Comput.*, 2025, **21**, 6226–6238.
17 A. P. Singh, H. Tanaka, Y. Miyazaki and W. Shinoda, *J. Phys. Chem. B*, 2025, **129**, 7939–7950.
18 C. Carucci, J. Philipp, J. A. Müller, A. Sudarsan, E. Kostyurina, C. E. Blanchet, N. Schwierz, D. F. Parsons, A. Salis and J. O. Rädler, *ACS Nano*, 2025, **19**, 10829–10840.
19 M. Ibrahim, J. Gilbert, M. Heinz, T. Nylander and N. Schwierz, *Nanoscale*, 2023, **15**, 11647–11656.
20 M. Grava, M. Ibrahim, A. Sudarsan, J. Pusterla, J. Philipp, J. O. Rädler, N. Schwierz and E. Schneck, *J. Chem. Phys.*, 2023, **159**, 154706.
21 M. P. K. Frewein, M. Rumetshofer and G. Pabst, *J. Appl. Crystallogr.*, 2019, **52**, 403–414.
22 G. Pabst, M. Rappolt, H. Amenitsch and P. Laggner, *Phys. Rev. E: Stat. Phys., Plasmas, Fluids, Relat. Interdiscip. Top.*, 2000, **62**, 4000–4009.
23 C. E. Blanchet, A. Spilotros, F. Schwemmer, M. A. Graewert, A. Kikhney, C. M. Jeffries, D. Franke, D. Mark, R. Zengerle, F. Cipriani, S. Fiedler, M. Roessle and D. I. Svergun, *J. Appl. Crystallogr.*, 2015, **48**, 431–443.
24 S. Haas, X. Sun, A. L. C. Conceição, J. Horbach and S. Pfeffer, *J. Synchrotron Radiat.*, 2023, **30**, 1156–1167.
25 P. Mariani, V. Luzzati and H. Delacroix, *J. Mol. Biol.*, 1988, **204**, 165–189.
26 M. Rappolt, A. Hodzic, B. Sartori, M. Ollivon and P. Laggner, *Chem. Phys. Lipids*, 2008, **154**, 46–55.
27 P. E. Harper, D. A. Mannock, R. N. Lewis, R. N. McElhaney and S. M. Gruner, *Biophys. J.*, 2001, **81**, 2693–2706.
28 M. J. Abraham, T. Murtola, R. Schulz, S. Páll, J. C. Smith, B. Hess and E. Lindahl, *SoftwareX*, 2015, **1–2**, 19–25.
29 S. Park, Y. K. Choi, S. Kim, J. Lee and W. Im, *J. Chem. Inf. Model.*, 2021, **61**, 5192–5202.
30 C. J. Dickson, B. D. Madej, Å. A. Skjevik, R. M. Betz, K. Teigen, I. R. Gould and R. C. Walker, *J. Chem. Theory Comput.*, 2014, **10**, 865–879.
31 W. L. Jorgensen, J. Chandrasekhar, J. D. Madura, R. W. Impey and M. L. Klein, *J. Chem. Phys.*, 1983, **79**, 926–935.
32 S. Mamatkulov and N. Schwierz, *J. Chem. Phys.*, 2018, **148**, 074504.
33 W. Humphrey, A. Dalke and K. Schulten, *J. Mol. Graphics*, 1996, **14**, 33–38.
34 R. J. Gowers, M. Linke, J. Barnoud, T. J. E. Reddy, M. N. Melo, S. L. Seyler, J. Domański, D. L. Dotson, S. Buchoux, I. M. Kenney and O. Beckstein, Proceedings of the 15th Python in Science Conference, 2016, pp. 98–105.
35 N. Michaud-Agrawal, E. J. Denning, T. B. Woolf and O. Beckstein, *J. Comput. Chem.*, 2011, **32**, 2319–2327.
36 ChemSketch, version 2022.1.2, Advanced Chemistry Development, Inc. (ACD/Labs), Toronto, ON, Canada, **https://www.acdlabs.com**, 2022.
37 SasView, version 6.0.0, **https://www.sasview.org**, accessed 24 October 2024.
38 B. Nagy, M. Campana, Y. N. Khaydukov and T. Ederth, *Langmuir*, 2022, **38**, 1725–1737.
39 M. W. Tate and S. M. Gruner, *Biochemistry*, 1989, **28**, 4245–4253.
40 D. Marsh, *Biophys. J.*, 2011, **101**, 2704–2712.
41 H. Petrache, S. Feller and J. Nagle, *Biophys. J.*, 1997, **72**, 2237–2242.